Composites Science and Technology 198 (2020) 108318

Contents lists available at ScienceDirect

Composites Science and Technology

journal homepage: http://www.elsevier.com/locate/compscitech

Reverse engineering of additive manufactured composite part by toolpath reconstruction using imaging and machine learning

Kaushik Yanamandra, Guan Lin Chen, Xianbo Xu, Gary Mac, Nikhil Gupta *

Composite Materials and Mechanics Laboratory, Mechanical and Aerospace Engineering Department, New York University, Tandon School of Engineering, Brooklyn, NY, 11201, USA

ARTICLE INFO

Keywords:
Additive manufacturing
3D printing
Fiber reinforced composite
Machine learning
Neural networks

ABSTRACT

Development of composite material parts requires significant research and development effort. The fiber size, volume fraction and direction are important in determining the properties of the part. Additive manufacturing (AM) methods are increasingly used for printing composite materials. Advancements in 3D scanning and imaging technology have raised a significant concern in reverse engineering of parts made by AM, which may result in counterfeiting and unauthorized production of high quality parts. This work is focused on using imaging methods and machine learning to reverse engineer a composite material part, where not only the geometry is captured but also the tool path of 3D printing is reconstructed using machine learning of microstructure. A dimensional accuracy with only 0.33% difference is achieved for the reverse engineered model.

1. Introduction

Additive Manufacturing (AM) methods are being adopted in industries ranging from aerospace, automotive and medical to arts and construction [1–3]. The capabilities of 3D printers are increasing to allow printing different kinds of materials and geometries. A wide range of feed materials are available across the spectrum of polymers, metals, ceramics and concrete as well as biomaterials and reinforced polymers [4–6]. 3D printed biomaterial such as strontium substituted hydroxyapatite (SrHA) recently showed promising results for bone tissue engineering applications [7].

Polymer matrix composites (PMCs) are now widely used in weight sensitive industrial applications such as aircraft and automobile structures. Many of these composite structures have been successfully 3D printed, especially with carbon and glass fiber reinforcement [8,9]. As the need for 3D printing lightweight materials is increasing, innovative material filaments are being developed for use in commercial 3D printers. A high-density polyethylene composite reinforced with fly ash cenosphere is found promising for use in commercial fused filament fabrication (FFF) 3D printers [10,11]. Efforts are also going on to recycle thermoplastics for developing high performance 3D printable PMC filaments for use in FFF printers [12]. These developments in new materials for AM are coupled with developing new capabilities in 3D printers. Using a multi-head FDM 3D printer has enabled co-deposition of multiple materials and printing multifunctional products [13]. FFF printing of carbon nanotube reinforced PEEK has also been used for developing multifunctional composites [14,15]. In many cases, the toolpath of 3D printers is configured to obtain specific distribution or orientation of reinforcement in the manufactured part.

Significant research and development effort is invested in developing the composite material parts using AM, which requires configuring parameters such as volume fraction and orientation of the reinforcement as well as optimizing AM parameters such as slicing thickness and toolpath [16]. Since many high technology applications, e. g. aircraft and satellite parts, are being printed using AM of composite materials, reverse engineering of these parts may result in loss of important intellectual property. The part shape can be reverse engineered using 3D scanners and CAD design tools. However, obtaining a high-quality composite part also requires reproducing composite parameters such as volume fraction of the reinforcement and 3D printer toolpath. Methods are available to determine the volume fraction and orientation of reinforcement in composites [17,18], which can also be used on 3D printed parts. In recent years, a steady improvement in the capabilities of micro-CT (μCT) scans is observed that has allowed improved image quality and possibility of conducting in-situ experiments [19–22]. In a recently published research article, micro-CT images are used to read the embedded QR code in a 3D printed part for product authentication and since the images are off low contrast image processing techniques were used to

* Corresponding author.
E-mail address: ngupta@nyu.edu (N. Gupta).

https://doi.org/10.1016/j.compscitech.2020.108318
Received 5 May 2020; Received in revised form 17 June 2020; Accepted 21 June 2020
Available online 28 June 2020

improve the readability [22]. The present work is focused on determining the possibility of reconstructing the toolpath of 3D printed parts by means of identifying the orientation of fibers in the microstructure obtained from microscopy and μCT scan, which has not been studied yet.

Cybersecurity risks related to sabotage or reverse engineering of parts have been studied in detail because 3D printing has made it easier to print parts without having expertise in the manufacturing process [23,24]. The classification of attack and possible damage by the attacks has been described for AM [25,26]. Once considered a remote possibility, side channel attacks related to capturing power consumption or vibration of the machine and using it for reverse engineering have been successfully demonstrated [27]. Since the AM process is defined as a cyber-physical system (CPS), it is exposed to both physical and cyber risks [28,29]. Sabotage during the 3D printing process has shown to embed defects that are hard to detect using conventional destructive or non-destructive test methods and cause in-service failure of parts [30]. Attacks related to sabotaging fiber reinforced laminated composite materials have also been studied, where a change in the layup sequence of a laminate can change the mechanical properties [31]. Technologies are required to enable positive identification of genuine parts made by AM [32]. Novel methods are being developed to counter the unauthorized production and reverse engineering. In one available approach, security features are embedded in CAD files so the high-quality part will only print under unique settings such as STL file resolution, slicing conditions, part orientation on the print bed, and the printer operating parameters [33]. In another approach, a method was developed using image processing techniques known as G-ID slicing and labelling interface [34]. Where the subtle patterns left by the 3D printer are identified and tagged using the slicing and infill parameters instead of embedding new tags onto the model [34]. In this work, the possibility of reverse engineering the tool path used to 3D print a composite material specimen is explored using machine learning methods. While ML methods are enabling composite material design [35–37], they may also be used for reverse engineering of products, which is the focus of the present work.

2. Material and methods

A FlashForge- Creator Pro Dual Extruder FFF 3D printer is used for printing the specimens. The CAD models are designed using SolidWorks 2017 (Waltham, Massachusetts) and saved in STL format. ABS-GF10 glass fiber reinforced acrylonitrile butadiene styrene (ABS) filament of 1.75 mm diameter, manufactured by 3DXTECH, Grand Rapids Michigan, USA, is used for 3D printing. The STL files are processed using ReplicatorG software for preparing the sliced model and generating the G-code, which is used for printing the model. The printing parameters included 100% solid infill, travel feed rate of 15 mm/s, feed rate of 41 mm/s, extrusion temperature of 220 °C, and build platform temperature of 120 °C. The printing direction of the fiber is set to 0° and 90° for alternative layers and the layer resolution (thickness of each layer) is set to 0.27 mm for the original model and 0.28 mm for the reversed engineered model. Fig. 1 shows the CAD model, a cube of 6 mm side, and Fig. 1 shows the μCT scan of the 3D printed model. Five identical cubes were printed for testing the repeatability of the process. Since the aim of the present work is to capture the fiber orientation information, the quality of the specimen and printing are not relevant at this stage. These aspects may be covered in the future works when proficiency in capturing the toolpath and printing parameters is attained.

2.1. Imaging

Hitachi S-3400N SEM (Tokyo, Japan) is used for capturing microstructure and dimensions of the specimens. The specimens are coated with gold using Cressington 108 Auto Sputter Coater (Watford, United Kingdom) before microscopy. The SEM images are used to measure the specimen height and the height of each layer, which are used as inputs in the ReplicatorG software when converting a 3D model into a STL format for printing.

The μCT scans are conducted using SkyScan 1172 (Bruker, Belgium) at the source voltage of 44 kV, current of 222 μA, and camera pixel size of 9.5 μm, rotation step of 0.6° per scan, and 360° rotation providing 656 raw images. The image reconstruction software has an option to rotate the images, which is useful in obtaining a clear final image of each layer and helps in obtaining the fiber orientation at each layer. This information of the fiber orientation at each layer is needed to reproduce the G-Code. The reconstructed μCT images of two layers are shown in Fig. 2. The glass fibers filled in ABS can be observed as the white lines. These fibers help in inferring the printing direction in each image. Here, the horizontal direction is taken as the reference and assigned 0° orientation and then the orientation of fibers in individual layers are identified in the counterclockwise direction.

2.2. Recurrent Neural Network

Recurrent neural network (RNN) is a supervised ML algorithm, which is designed to model sequential data. The order is very important in sequential data. There are different forms of sequence modeling algorithms but the one used here is the many-to-one sequence model,

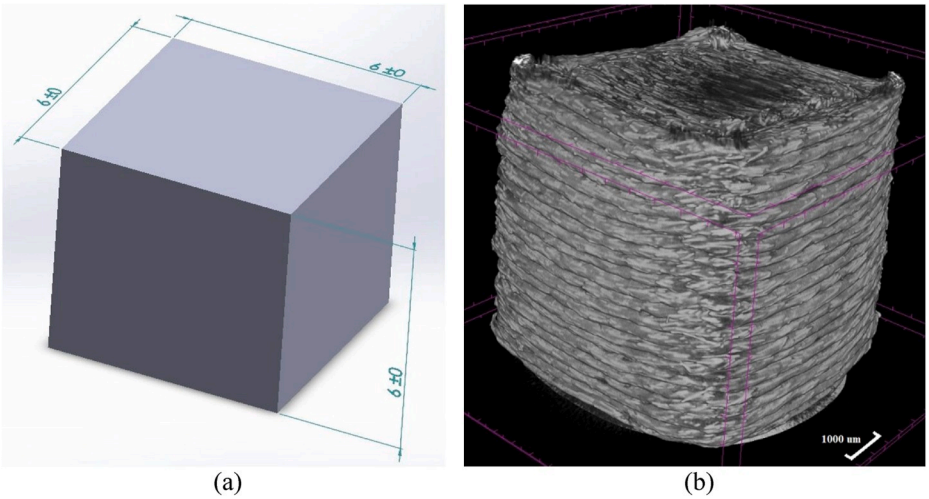

(a) (b)

Fig. 1. (a) CAD model with dimensions marked in mm and (b) μCT scan of the 3D printed part (the violet lines seen in the image are from the imaging reference frame).

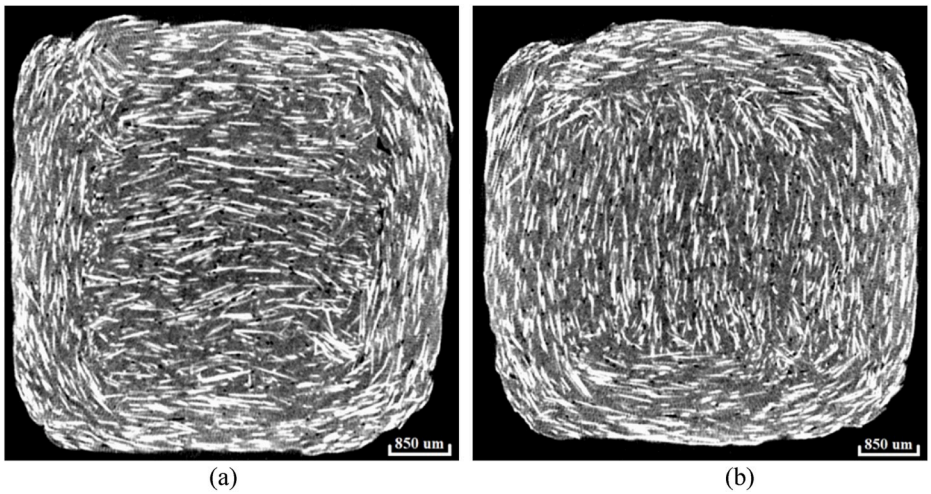

Fig. 2. CT scan of slices of a 3D printed model after reconstruction showing (a) 0° and (b) 90° orientation of the fiber in the middle part.

which implies that the input data is a sequence but the output is not a sequence, rather a fixed-size vector. In a standard neural network, after the model is trained, information flows from input to the hidden layer to the output layer. In an RNN, the hidden layer has inputs from both the input layer and the hidden layer from the previous step. The flow of information in an RNN from one time-step to another introduces memory of past inputs into the network [38–40]. This flow of information is usually depicted as a loop called recurrent edge.

The representation of a multilayer RNN is presented in Fig. 3, which is used to predict the direction of fibers in a μCT scan image. The input represented as $x^{(t)}$ is the CT-scan image in the present case and the output $y^{(t)}$ is the fiber orientation angle. The curved loops beside the hidden layers $h_1^{(t)}$ and $h_2^{(t)}$ in the figure represent the recurrent edge. The unfolded version shows the functioning of recurrent edge, where the information flows from the past inputs to the hidden layer. At any time instance t the model uses the information from the past and input at time t to predict the output at t. Since AM follows a sequential process of printing, the fiber orientation at each layer can be helpful to predict the orientation of fiber of the next layer. Using this idea, an RNN model is implemented in Python language and TensorFlow package. Typically, a backpropagation through time (BPTT) algorithm is used to train an RNN. However, the BPTT algorithm sometimes has a problem of vanishing gradient while training RNN. Since sequential data is fed into the RNN model for training, it faces difficulty in learning the long-term dependencies, which implies that the model will not be able to relate the images which occurred several time steps apart. This problem leads to preventing the weights in the hidden layer from updating according to the gradient from the earlier time step, causing the RNN to stop from further training. To address these issues, the RNN architecture with Long Short-Term Memory (LSTM) network is used [40]. RNN with hidden layers containing LSTM cells take information from the input and from the previous hidden layers and calculate the output through a standard set of equations. Then sending the information to the next layer in the model and to the hidden layer (i.e. another LSTM cell) in the next time step. LSTM cells are designed to handle the vanishing gradient problem, which have inbuilt default units programmed to remember the updates from the previous time steps without loss of information over long time steps.

3. Results and discussion

3.1. Dimensional accuracy of reverse engineered sample

The printed cubes have some curvature due to thermal expansion mismatch between the modeling material and build plate. Hence, dimensional measurements were conducted on the printed cubes and on the images obtained by SEM to measure the length of various sections.

Table 1
Comparison of measurements of one of the original models obtained using Vernier calipers and SEM images.

Measurement	Length (mm)	Width (mm)	Height (mm)
Vernier Caliper	6.06 ± 0.04	6.10 ± 0.04	6.06 ± 0.08
SEM	6.05 ± 0.01	6.10 ± 0.04	6.10 ± 0.02

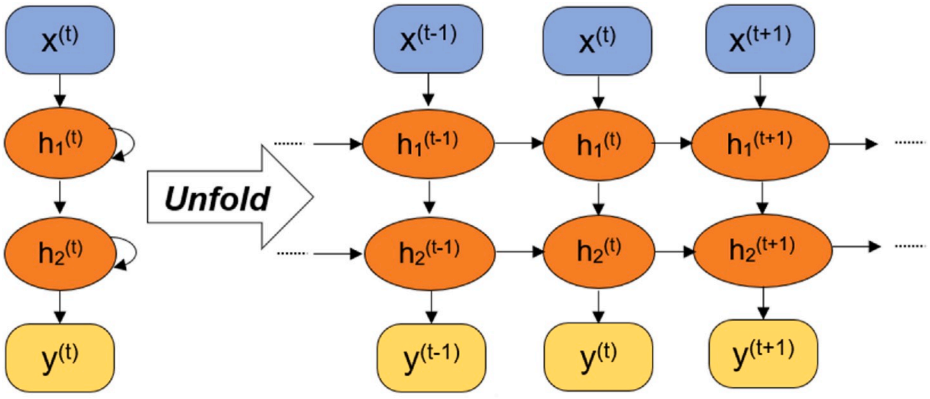

Fig. 3. Representation of the multilayer RNN and the unfolded version of it.

Table 1 compares the measurements obtained by the two methods. The measurements obtained from both methods are very consistent and have a small standard deviation. The measured dimensions are consistent with those in the CAD model. After finding the overall dimensions, the next task in reverse engineering is to gather information on the number of layers in the specimen and fiber orientation in each step.

The fiber orientation is obtained from the μCT scan images. In Fig. 4, images of the 3D printed model are shown. It can be observed that a border is first printed and then the material is deposited to fill the inner square space. This region of interest is enclosed by the red squares, in which glass fibers are aligned in a specific direction only. The orientations of fibers are identified as 0° and 90° in Fig. 4a and Fig. 4b, respectively. Similar analysis is conducted layer by layer and these μCT images are used to train the ML model. The boundary is ignored in the analysis because the direction of boundary printing is always the same and easy to replicate.

A few μCT images show overlapping printing directions as shown in Fig. 5 because the scan resolution is much finer than the deposited layer thickness. These overlapping images are mostly at the boundary of two deposited layers due to the slight slope that can be either in the printing or in the specimen positioning on the μCT stage. These images are removed from the dataset because there is enough information available from other slices that are cleaner. In order to have a defined/labeled angle, a set of 433 images that show clear orientation of fibers is identified and rotated so that the fiber orientation is horizontal. These images are labeled as 0° fiber orientations. All the images are cropped to a region of interest to decrease the number of pixels in the analysis. The cropped image is shown in Fig. 5 with each image having 536 × 536 pixels. A circular cropped image is used in order to avoid any sharp angles in the image because training a neural network having corners or sharp angles can make the network biased resulting in inaccurate predictions. Individual fibers in each image show some variation in their direction. However, the algorithm takes the global signature as the features for the 0° and disregards the individual fiber orientation. Each of these images are then rotated counterclockwise from 0° to 180° at 1°interval using a Python code. This procedure allows creating a large training database with controlled fiber orientation and trains the model to identify any angle. This procedure resulted in 78,373 images. The process of rotating the images and cropping them to generate training data is known as image augmentation and it is helpful in training the neural network model to be robust.

In order to accelerate the image augmentation, Binarized Statistical Image Features (BSIF) algorithm is used [41]. BSIF is used to convert an image into a binary image format without losing valuable features. Fig. 6 shows an example of the image produced by the BSIF algorithm. The images processed through BSIF algorithm are used for training the ML algorithm. The output image produced by the BSIF algorithm is binary code for each pixel in the image and is stored in a 1D array, which makes it convenient to handle large amounts of data. Although the visual representation of features in Fig. 6 is not well resolved to the naked eye, such images are proven to perform as well as any other state-of-the-art descriptor [41]. Use of BSIF code reduced each image to 1 × 256 pixels, which reduced the computational expense involved in running RNN.

3.2. Prediction of fiber orientation

The RNN algorithm is trained using the 78,373 images generated in the previous step to predict the orientation/angle of the fiber. The dataset is split into 70% (54,861 images) for training and 30% (23,512 images) of validation. In addition, a test dataset of 5,250 μCT scan images is generated as a test dataset to check the accuracy of prediction after training. The mean square error (MSE) loss function is used in this algorithm since the output value is a continuous number between 0° and 180°. Once the training of the neural network is started, it is run iteratively and the best output for each iteration is saved. When the least MSE is obtained, then the architecture of the neural network is finalized, and the test dataset is used to run through the RNN model. It is important to limit the number of times the algorithm runs on the test dataset because RNN can remember the data, which affects the accuracy of the model.

In Table 2, the MSE values for training, validation and test dataset at different epochs is shown. Epoch is the number of times the training dataset is run iteratively to train the model. As the number of epochs increases, the performance on the test dataset improves which is evident. However, as the number of epochs increases, the time required to run the algorithm also increases so it is important to find a balance between the computing time and the accuracy. Here, the training of the model for 10,000 epochs took about 31 h and it achieved the lowest MSE for the test dataset. As the importance was given for accuracy, 10,000 epochs were used for predicting the angle. The trend presented in Table 2 shows that further training will increase the expense without increasing the accuracy by any appreciable extent. Fig. 7 shows a graph between MSE values for each angle in the training and test dataset for the model trained for 10000 epochs. The test shows improved accuracy over training dataset. The MSE values for the training and test dataset for 10,000 epochs are very close. The trend observed in Fig. 7 does not show signs of overfitting or underfitting. Fig. 7(a) shows the prediction of the fiber angle with respect to the actual angle for the test dataset. The predicted value for each labeled angle and the linear regression line is also shown in the graph. As can be observed in Fig. 7(b), the result

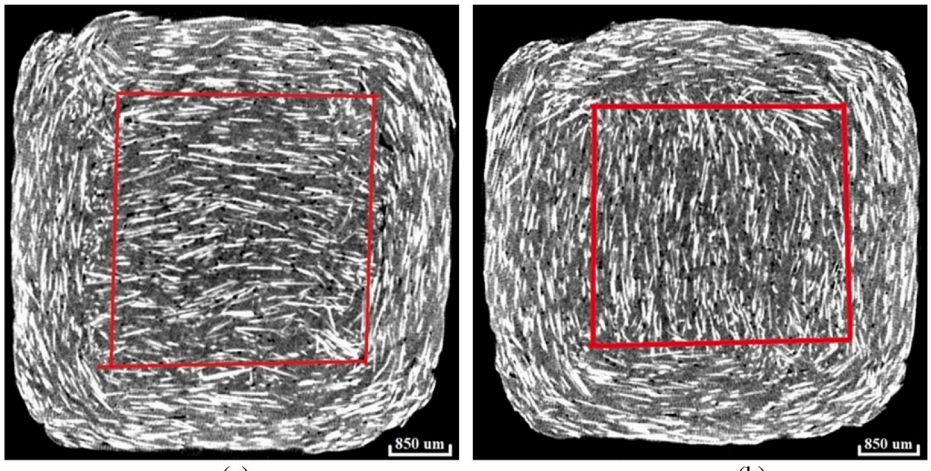

Fig. 4. Image slices of a 3D printed model showing a region of interest in (a) 0° and (b) 90° fiber orientation in the infill.

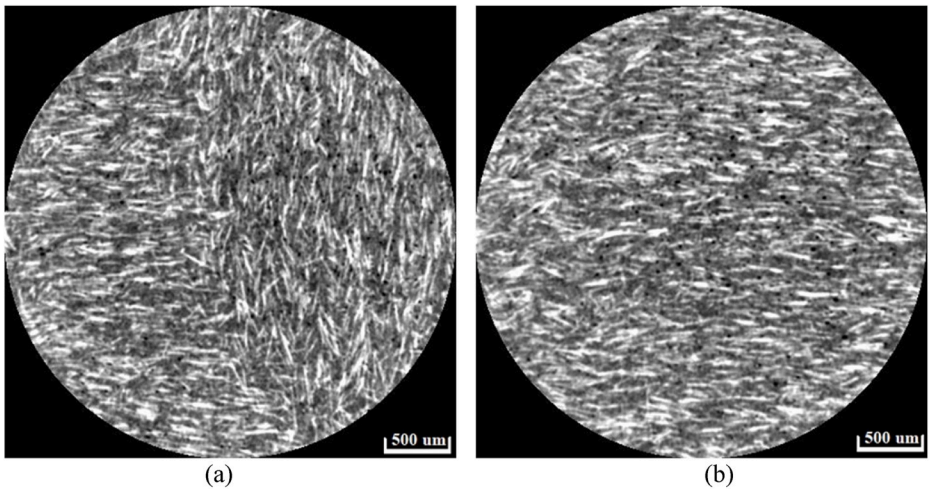

Fig. 5. μCT scan images showing (a) a region of overlapping layers and (b) the region of interest selected in the slice, which is sent to the BSIF algorithm.

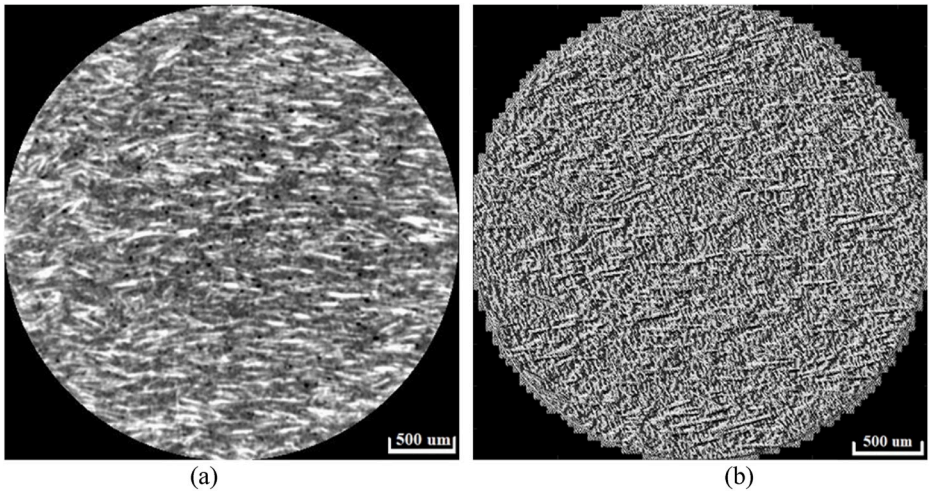

Fig. 6. μCT scan image (a) before going though BSIF and (b) the image produced by BSIF algorithm.

Table 2
MSE values at different epochs for Training, Validation and Test Datasets.

Parameter	Epochs		
	500	1000	10000
Training MSE	0.49	0.23	0.06
Validation MSE	1.53	1.45	0.04
Test MSE	6.40	6.20	0.04

predicted by the algorithm is very close to the exact angle with less than 0.5° variation. All the points lie around the regression line and MSE values are low. But at the ends of the regression line that is at 0° and 180° where the predicted angles are deviating away from the regression line, the error in prediction increases which is evident in Fig. 7 (a) which shows higher MSE values compared to other angles. This is because the fibers oriented at both these angles appear the same which makes it difficult for the ML algorithm to learn and predict accurately. Therefore, the prediction error is higher for 0° and 180° angles. From this analysis, the orientation of the fiber at each layer of the 3D model can be predicted from a μCT scan image of the model.

3.2.1. Validation of the machine learning model

For validating the ML model used, images obtained on a 3D printed cylindrical specimen are used to predict the fiber orientation. Fig. 8(a) the model of the cylinder in Solidworks is shown and in Fig. 8(b) the μCT scan image of the slice of 3D printed cylinder can be seen. In Fig. 8, MSE for the training and test sets is plotted. It is observed that the MSE is very low, which is also reflected in the angle prediction plotted in Fig. 8. This test on a different specimen demonstrates that the trained ML algorithm is capable of predicting the fiber orientation in similar specimens.

3.2.2. 3D printing of reverse engineered model

Using the information from previous analysis for the cube, the reverse engineered model is designed in SolidWorks 2017. The measured length, width and height values of 6.05, 6.10 and 6.09 mm, respectively are used as the model dimensions and then G-code is generated using the measured layer thickness and fiber orientation. A comparison of original and reverse engineered specimen dimensions is presented in Table 3. The dimensions of both types of specimens show only 0.33% difference. The values presented in this table are obtained on 5 original and 10 reverse engineered specimens and several measurements are taken on each specimen at different locations. The dimensions of the reverse engineered model are observed to be slightly higher than the original 3D printed specimens but the difference is only 0.33%. These results show that the available ML methods can be trained to predict the fiber angle in fiber reinforced composites and develop reverse engineered components.

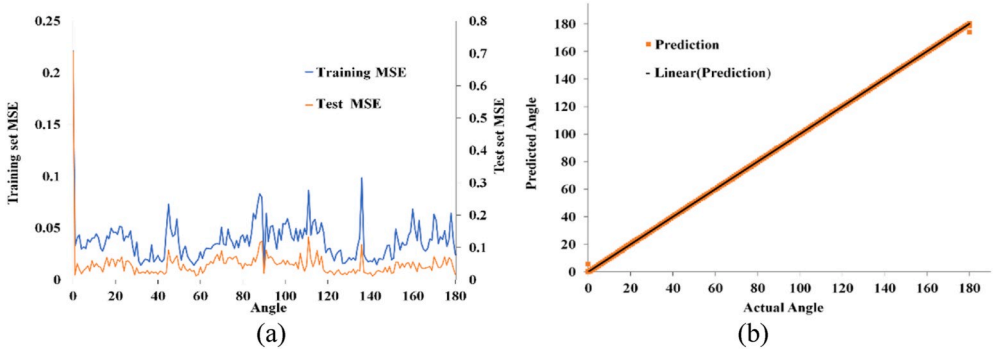

Fig. 7. (a) Mean square error for each angle in the training and test dataset. (b) The predicted angle of fiber orientation compared to the correct labeled value for test dataset with the regression line.

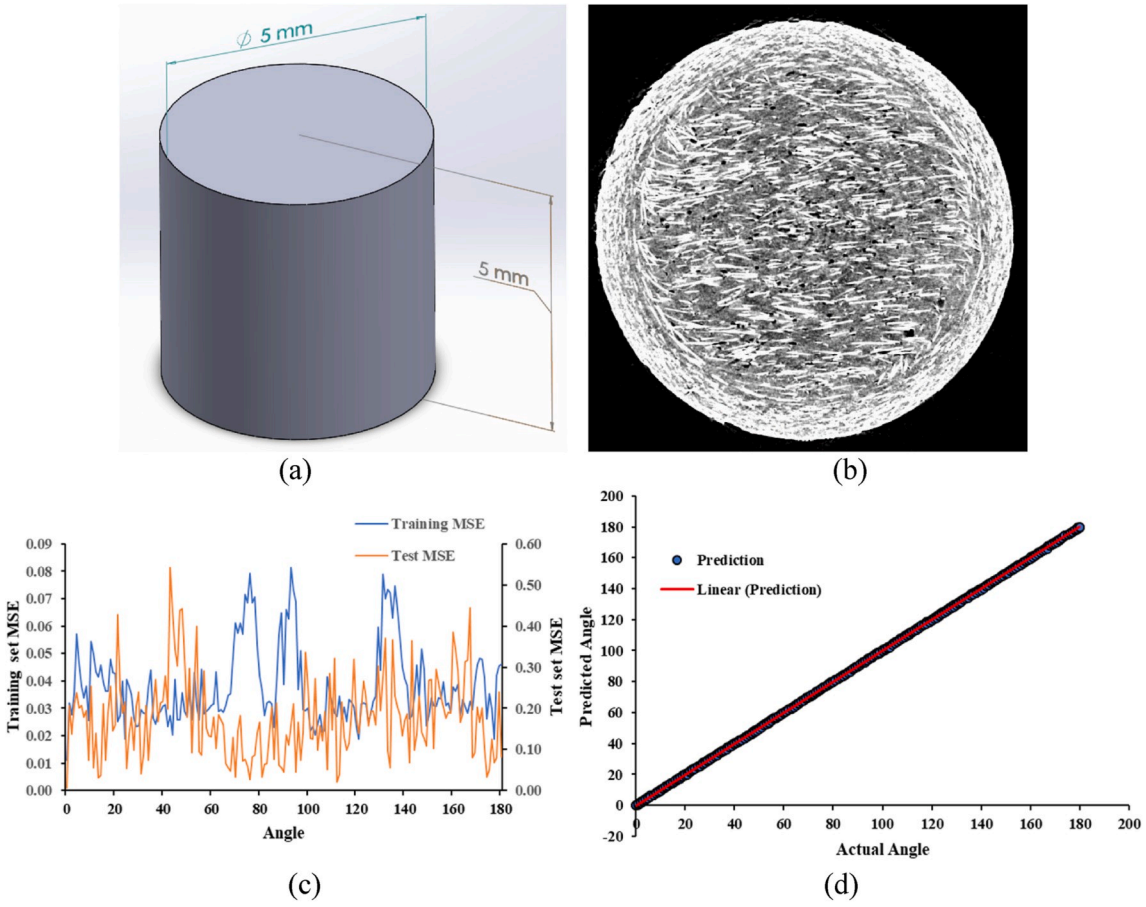

Fig. 8. (a) Model of the cylinder made in SolidWorks, (b) micro CT-scan image of a slice of cylinder used for machine learning. (c) Mean Square error for each angle in the training and test datasets. (d) The predicted angle of fiber orientation compared to the correct labeled value for test dataset with the regression line.

Table 3
Measurements of original and reverse engineered model.

Dimension	Original (mm)	Reverse Engineered (mm)	Difference (%)
Length	6.08 ± 0.04	6.10 ± 0.03	0.33
Width	6.13 ± 0.02	6.15 ± 0.02	0.32
Height	6.07 ± 0.05	6.09 ± 0.02	0.33

4. Conclusions

The aim of this work is to reverse engineer a high-quality replica of fiber reinforced composite material. A glass fiber reinforced ABS filament is used to 3D print the specimens.

- A reverse engineering method is proposed using the μCT scan and SEM images of the model. The tool-path information is captured by identifying the fiber orientation in each layer with the help of Recurrent Neural Network with LSTM architecture.
- A refined RNN model achieving a high degree of accuracy that has MSE loss of 0.04 an error of 0.5° in predicting the printing orientation of the fiber is obtained. By using RNN architecture, the printing orientation at each layer of the model was successfully identified.
- The original models were reverse engineered with a dimensional accuracy difference of only 0.33%.

The work shows that the capabilities developed for designing high performance composites can also be used for reverse engineering high quality replicas of composite parts. The research on developing configurations of composite layup sequence for certain parts can be reverse engineered from the microstructural images. Although the part geometry is simple in the current example, the success of the ML method in identifying tracking any given orientation of the fibers demonstrates the possibility of reconstructing the G-code and reverse engineering any composite part.

Declaration of competing interest

The authors declare that they have no known competing financial interests or personal relationships that could have appeared to influence the work reported in this paper.

CRediT authorship contribution statement

Kaushik Yanamandra: Conceptualization, Investigation, Validation, Writing - original draft. **Guan Lin Chen:** Investigation, Formal analysis. **Xianbo Xu:** Conceptualization, Methodology. **Gary Mac:** Writing - review & editing. **Nikhil Gupta:** Conceptualization, Writing - original draft, Supervision, Funding acquisition.

Acknowledgments

The work is supported by National Science Foundation SaTC-EDU grant DGE-1931724. The authors thank NYU Tandon Makerspace for facilities and support provided.

Appendix A. Supplementary data

Supplementary data to this article can be found online at https://doi.org/10.1016/j.compscitech.2020.108318.

References

[1] M. George, K.R. Aroom, H.G. Hawes, B.S. Gill, J. Love, 3D printed surgical instruments: the design and fabrication process, World J. Surg. 41 (2017) 314–319.
[2] S. Singamneni, L. Yifan, A. Hewitt, R. Chalk, W. Thomas, Additive manufacturing for the aircraft industry: a review, J. Aeronaut. Aero. Eng. 8 (2019) 2.
[3] R. Leal, F. Barreiros, L. Alves, F. Romeiro, J. Vasco, M. Santos, C. Marto, Additive manufacturing tooling for the automotive industry, Int. J. Adv. Manuf. Technol. 92 (2017) 1671–1676.
[4] T.D. Ngo, A. Kashani, G. Imbalzano, K.T.Q. Nguyen, D. Hui, Additive manufacturing (3D printing): a review of materials, methods, applications and challenges, Compos. B Eng. 143 (2018) 172–196.
[5] J. Justo, L. Távara, L. García-Guzmán, F. París, Characterization of 3D printed long fibre reinforced composites, Compos. Struct. 185 (2018) 537–548.
[6] J.M. Koo, J. Kang, S.-H. Shin, J. Jegal, H.G. Cha, S. Choy, M. Hakkarainen, J. Park, D.X. Oh, S.Y. Hwang, Biobased thermoplastic elastomer with seamless 3D-Printability and superior mechanical properties empowered by in-situ polymerization in the presence of nanocellulose, Compos. Sci. Technol. 185 (2020) 107885.
[7] D. Pierantozzi, A. Scalzone, S. Jindal, L. Stīpniece, K. Šalma-Ancāne, K. Dalgarno, P. Gentile, E. Mancuso, 3D printed Sr-containing composite scaffolds: effect of structural design and material formulation towards new strategies for bone tissue engineering, Compos. Sci. Technol. 191 (2020) 108069.
[8] X. Wang, M. Jiang, Z. Zhou, J. Gou, D. Hui, 3D printing of polymer matrix composites: a review and prospective, Compos. B Eng. 110 (2017) 442–458.
[9] M. Heidari-Rarani, M. Rafiee-Afarani, A.M. Zahedi, Mechanical characterization of FDM 3D printing of continuous carbon fiber reinforced PLA composites, Compos. B Eng. 175 (2019) 107147.
[10] A.K. Singh, B. Patil, N. Hoffmann, B. Saltonstall, M. Doddamani, N. Gupta, Additive manufacturing of syntactic foams: Part 1: development, properties, and recycling potential of filaments, JOM (J. Occup. Med.) 70 (2018) 303–309.
[11] A.K. Singh, B. Saltonstall, B. Patil, N. Hoffmann, M. Doddamani, N. Gupta, Additive manufacturing of syntactic foams: Part 2: specimen printing and mechanical property characterization, JOM (J. Occup. Med.) 70 (2018) 310–314.
[12] N. Singh, D. Hui, R. Singh, I.P.S. Ahuja, L. Feo, F. Fraternali, Recycling of plastic solid waste: a state of art review and future applications, Compos. B Eng. 115 (2017) 409–422.
[13] D.G. Bekas, Y. Hou, Y. Liu, A. Panesar, 3D printing to enable multifunctionality in polymer-based composites: a review, Compos. B Eng. 179 (2019) 107540.
[14] M.F. Arif, H. Alhashmi, K.M. Varadarajan, J.H. Koo, A.J. Hart, S. Kumar, Multifunctional performance of carbon nanotubes and graphene nanoplatelets reinforced PEEK composites enabled via FFF additive manufacturing, Compos. B Eng. 184 (2020) 107625.
[15] A. Mora, P. Verma, S. Kumar, Electrical conductivity of CNT/polymer composites: 3D printing, measurements and modeling, Compos. B Eng. 183 (2020) 107600.
[16] J. Kiendl, C. Gao, Controlling toughness and strength of FDM 3D-printed PLA components through the raster layup, Compos. B Eng. 180 (2020) 107562.
[17] W. McDonough, J. Dunkers, K. Flynn, D. Hunston, A test method to determine the fiber and void contents of carbon/glass hybrid composites, J. ASTM Int. (JAI) 1 (2004) 1–15.
[18] B.R. Denos, D.E. Sommer, A.J. Favaloro, R.B. Pipes, W.B. Avery, Fiber orientation measurement from mesoscale CT scans of prepreg platelet molded composites, Compos. Appl. Sci. Manuf. 114 (2018) 241–249.
[19] S.C. Garcea, Y. Wang, P.J. Withers, X-ray computed tomography of polymer composites, Compos. Sci. Technol. 156 (2018) 305–319.
[20] Y. Chai, Y. Wang, Z. Yousaf, N.T. Vo, T. Lowe, P. Potluri, P.J. Withers, Damage evolution in braided composite tubes under torsion studied by in-situ X-ray computed tomography, Compos. Sci. Technol. 188 (2020) 107976.
[21] H.K. Bas, W. Jin, N. Gupta, R.K. Behera, In-situ micro-CT characterization of mechanical properties and failure mechanism of cementitious syntactic foams, Cement Concr. Compos. 90 (2018) 50–60.
[22] F. Chen, J. Zabalza, P. Murray, S. Marshall, J. Yu, N. Gupta, Embedded product authentication codes in additive manufactured parts: imaging and image processing for improved scan ability, Addit. Manuf. 35 (2020) 101319.
[23] S.E. Zeltmann, N. Gupta, N.G. Tsoutsos, M. Maniatakos, J. Rajendran, R. Karri, Manufacturing and security challenges in 3D printing, JOM (J. Occup. Med.) 68 (2016) 1872–1881.
[24] N. Gupta, A. Tiwari, S.T.S. Bukkapatnam, R. Karri, Additive manufacturing cyber-physical system: supply chain cybersecurity and risks, IEEE Access 8 (2020) 47322–47333.
[25] M. Yampolskiy, W.E. King, J. Gatlin, S. Belikovetsky, A. Brown, A. Skjellum, Y. Elovici, Security of additive manufacturing: attack taxonomy and survey, Addit. Manuf. 21 (2018) 431–457.
[26] D.R. Safford, M. Wiseman, Hardware rooted trust for additive manufacturing, IEEE Access 7 (2019) 79211–79215.
[27] S.-Y. Yu, A.V. Malawade, S.R. Chhetri, M.A. Al Faruque, Sabotage attack detection for additive manufacturing systems, IEEE Access 8 (2020) 27218–27231.
[28] L.M.G. Graves, J. Lubell, W. King, M. Yampolskiy, Characteristic aspects of additive manufacturing security from security awareness perspectives, IEEE Access 7 (2019) 103833–103853.
[29] M. Yampolskiy, W. King, G. Pope, S. Belikovetsky, Y. Elovici, Evaluation of Additive and Subtractive Manufacturing from the Security Perspective, Springer International Publishing, Cham, 2017, pp. 23–44.
[30] S. Belikovetsky, M. Yampolskiy, J. Toh, J. Gatlin, Y. Elovici, dr0wned-cyber-physical attack with additive manufacturing, in: Proceedings of the 11th USENIX Conference on Offensive Technologies, USENIX Association, Vancouver, BC, Canada, 2017, p. 1.
[31] B. Ranabhat, J. Clements, J. Gatlin, K.-T. Hsiao, M. Yampolskiy, Optimal sabotage attack on composite material parts, Int. J. Crit. Infrastruct. Protect. 26 (2019) 100301.
[32] F. Chen, Y. Luo, N.G. Tsoutsos, M. Maniatakos, K. Shahin, N. Gupta, Embedding tracking codes in additive manufactured parts for product authentication, Adv. Eng. Mater. 21 (2019) 1800495.
[33] F. Chen, G. Mac, N. Gupta, Security features embedded in computer aided design (CAD) solid models for additive manufacturing, Mater. Des. 128 (2017) 182–194.
[34] M.D. Dogan, F. Faruqi, A.D. Churchill, K. Friedman, L. Cheng, S. Subramanian, S. Mueller, G-ID: Identifying 3D prints using slicing parameters, in: Proceedings of the 2020 CHI Conference on Human Factors in Computing Systems, Association for Computing Machinery, Honolulu, HI, USA, 2020, pp. 1–13.
[35] C.-T. Chen, G.X. Gu, Machine learning for composite materials, MRS Commun. 9 (2019) 556–566.
[36] R. Liu, Y.C. Yabansu, A. Agrawal, S.R. Kalidindi, A.N. Choudhary, Machine learning approaches for elastic localization linkages in high-contrast composite materials, Integrating Mater. Manuf. Innovat. 4 (2015) 192–208.
[37] H. Liu, S. Liu, Z. Liu, N. Mrad, H. Dong, Prognostics of Damage Growth in Composite Materials Using Machine Learning Techniques, IEEE International Conference on Industrial Technology (ICIT), 2017, pp. 1042–1047, 2017.
[38] M. Boden, A Guide to Recurrent Neural Networks and Backpropagation, the Dallas project, 2002.
[39] S. Raschka, V. Mirjalili, Python Machine Learning: Machine Learning and Deep Learning with Python, Scikit-Learn, and TensorFlow 2, Packt Publishing Ltd, 2019.
[40] H. Sak, A.W. Senior, F. Beaufays, Long Short-Term Memory Recurrent Neural Network Architectures for Large Scale Acoustic Modeling, 2014.
[41] J. Kannala, E. Rahtu, BSIF: Binarized statistical image features, in: Proceedings of the 21st International Conference on Pattern Recognition, ICPR2012, 2012, pp. 1363–1366.